Available online at www.sciencedirect.com
SciVerse ScienceDirect
Acta Materialia 60 (2012) 2637–2646
Acta MATERIALIA
www.elsevier.com/locate/actamat

Role of crystal defects on brittleness of C15 Cr_2Nb Laves phase

Z.Q. Yang [a,b,*], M.F. Chisholm [b], B. Yang [a], X.L. Ma [a], Y.J. Wang [a], M.J. Zhuo [a], S.J. Pennycook [b]

[a] Shenyang National Laboratory for Materials Science, Institute of Metal Research, Chinese Academy of Sciences, Shenyang 110016, China
[b] Materials Science and Technology Division, Oak Ridge National Laboratory, Oak Ridge, TN 37831, USA

Received 2 December 2011; received in revised form 18 January 2012; accepted 19 January 2012
Available online 1 March 2012

Abstract

First-principles calculations, high-resolution transmission electron microscopy (HRTEM) investigations and geometrical phase analysis of lattice strain based on HRTEM images have been carried out on C15 Cr_2Nb Laves phase. Asymmetrical nanoscale regions with severe lattice distortion were observed in the vicinity of Shockley partial dislocation cores. These disturbed regions are the result of synchroshear inside the Nb–Cr–Nb triple layers. Reactions of dislocations with twin boundaries (TBs) also result in severe lattice distortion. The resulting local lattice distortion and perturbed strain field deleteriously impact dislocation-governed plasticity. First-principles calculations show that cleavage occurs preferentially between the single Cr layer and the Nb–Cr–Nb triple layer in these materials. TBs, which are on single Cr layers, nucleate and propagate cracks readily in Cr_2Nb, as evidenced by the lattice dilatation along a TB interacting with one 60° dislocation. The present study shows atomic level evidence on how crystal defects and their interactions influence the mechanical properties, especially the poor toughness at low temperatures, of C15 Cr_2Nb. This provides new insights into the origin of low temperature brittleness of Laves compounds with complex structures.
© 2012 Acta Materialia Inc. Published by Elsevier Ltd. All rights reserved.

Keywords: Laves phase; Dislocation; Twin boundary; Fracture; Brittleness

1. Introduction

Laves phase intermetallics are potential high-temperature structural materials because of their high melting temperatures, fairly low mass densities, reasonable oxidation resistance and strong intrinsic resistance to creep deformation [1–3]. Face-centered cubic (fcc) C15 Laves phases are expected to show better plastic deformability than the other two Laves phases of hexagonal C14 and C36, since more slip systems are available in fcc structures. The Cl5 Laves phases are thus of particular interest and have been subjected to extensive experimental and theoretical studies [3–14]. Stoichiometric Cr_2Nb is a C15 Laves compound that is stable at ambient temperature [6,14]. However, even the fcc Laves phases, including the C15 Cr_2Nb, are not yet widely exploited structural materials in industrial technology, due to their pronounced brittleness at low temperatures [3,7]. This obstacle has evoked an upsurge of research interest in the deformation properties of the Laves phases, in order to overcome their poor damage tolerance [3].

Most Laves phases are brittle up to high homologous temperatures [15,16]. The C15 Cr_2Nb has a large Poisson's ratio of ~0.34, suggesting non-directional atomic bonding [11], in contrast to other intermetallics (like NiAl [17]) with a covalent component to the bonding which influences dislocation mobility and thus results in the poor ductility. Therefore, the poor ductility of the C15 Cr_2Nb is expected to be more closely related to crystal defects in these materials, since the atomic bonding is non-directional [11]. Dislocations are expected to move with substantial

* Corresponding author at: Shenyang National Laboratory for Materials Science, Institute of Metal Research, Chinese Academy of Sciences, Shenyang 110016, China. Tel.: +86 24 83978275; fax: +86 24 23971215.
E-mail address: yangzq34@yahoo.com (Z.Q. Yang).

1359-6454/$36.00 © 2012 Acta Materialia Inc. Published by Elsevier Ltd. All rights reserved.
doi:10.1016/j.actamat.2012.01.030

difficulty in these compounds with a complex crystal structure. This property is responsible for the materials' excellent high-temperature strength and creep resistance, but may also be responsible for their low temperature brittleness. In C15 Cr_2Nb samples deformed at high temperatures, dislocations, twins and stacking faults (SFs) have been characterized by transmission electron microscopy (TEM) [3,5,7,18], showing the occurrence of numerous interactions and reactions between perfect dislocations, Shockley partials and twin boundaries (TBs). Cracking may initiate at intersections of dislocation bands, like in MgO [19]. Fracture may occur in some materials where the TB is weak and propagates a crack readily, like natural corundum [20] and Mg alloys [21]. However, it is still less understood how the various crystal defects interact with each other, and how their interactions and/or reactions influence the mechanical performance of the C15 Cr_2Nb compound, which are key requirements for understanding the origin of the low temperature brittleness.

In the present study, high-resolution TEM (HRTEM) observations were carried out to investigate the atomic scale structures of crystal defects and related nanoscale structural evolutions. Geometric phase analysis (GPA) was applied to quantify the lattice distortion induced by crystal defects and their interactions in the C15 Cr_2Nb. Asymmetrical strain fields around partial dislocations and large lattice dilatation along TBs interacting with dislocations were observed and quantified. First-principles calculations were also performed in order to obtain some in-depth understanding of the experimental observations. These atomic scale findings suggest that crystal defects and their interactions have intimate relation with the poor damage tolerance of C15 Cr_2Nb.

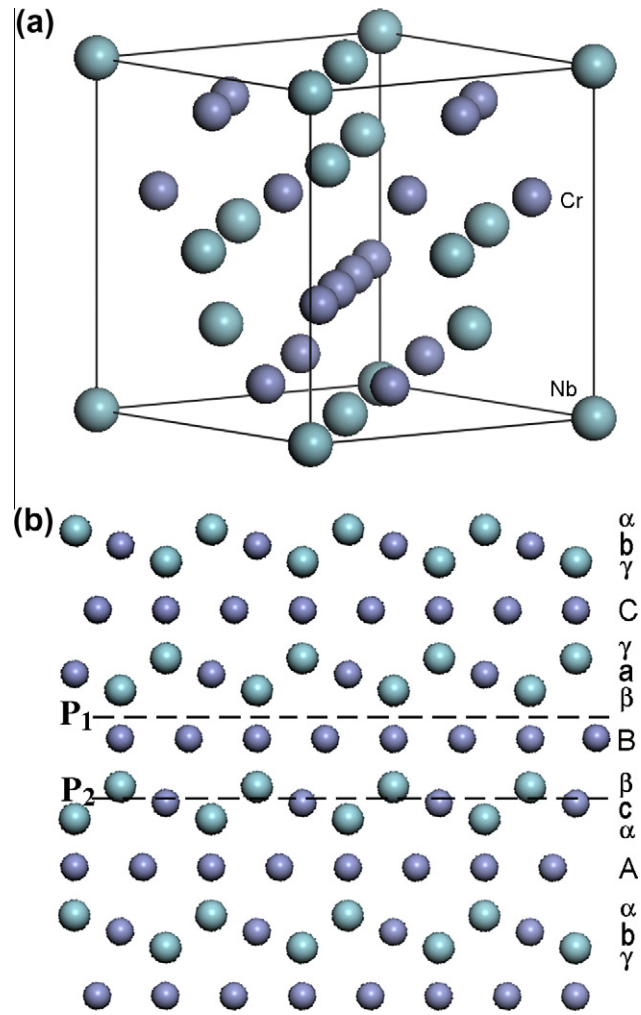

Fig. 1. (a) Unit cell of the C15 Cr_2Nb and (b) $[\bar{1}\,1\,0]$ projection showing stacking of the single Cr layers and triple Nb–Cr–Nb layers. P_1 and P_2 indicate two possible cleavage positions.

2. Experiments and calculations

2.1. Material and microstructural characterization

Cr_2Nb ingots were prepared by vacuum arc-melting from high-purity Cr and Nb. The ingots were slowly cooled in air to room temperature. Samples for TEM observations were prepared by Ar ion milling after mechanical polishing. The TEM, HRTEM and high-resolution scanning-transmission electron microscopy (HRSTEM) observations were performed on a Tecnai F30 microscope. The HRTEM images were recorded using a $2k \times 2k$ CCD camera along the zone axis of $[\bar{1}\,1\,0]$. The C15 Cr_2Nb belongs to the space group $Fd\bar{3}m$, with niobium and chromium at $2a$ and $4d$ sites of $(0,0,0)$ and $(5/8,5/8,5/8)$, respectively. Fig. 1 shows a unit cell and the $[\bar{1}\,1\,0]$ projection of the C15 Cr_2Nb. The (1 1 1) plane stacking in the C15 structure consists of single layers A, B and C, composed of pure Cr atoms, and triple layers $\boldsymbol{\alpha c \beta}$, $\boldsymbol{\beta a \gamma}$ and $\boldsymbol{\gamma b \alpha}$, composed of a layer (**a**, **b** or **c**) of small Cr atoms sandwiched between two layers of large Nb atoms ($\boldsymbol{\alpha}$, $\boldsymbol{\beta}$ or $\boldsymbol{\gamma}$). Fig. 2a is a TEM image with a selected area electron diffraction (SAED) pattern, revealing microtwins in the C15 Cr_2Nb. Fig. 2b is an HRSTEM image for a TB region, demonstrating that the boundary sits on the pure Cr (1 1 1) single plane, as indicated by the $[\bar{1}\,1\,0]$ atomic projection overlapped on the image. The atomic lattice on the left side of the TB is not as clear and sharp as that on the right side, which is due to a slight deviation from the $[\bar{1}\,1\,0]$ zone axis caused by either local sample bending in the thin region of the TEM sample, or lattice distortion induced by other crystal defects.

2.2. Quantitative HRTEM

To enable interpretation of experimental HRTEM images, image simulations were performed using the multislice algorithm as implemented by the software package EMS [22]. The method of GPA, developed by Hÿtch et al. [23], is a powerful tool for measuring strains quantitatively as revealed in HRTEM micrographs. It has been shown that strain measurements obtained by this method agree well with theoretical calculations based on linear anisotropic elastic theory to an accuracy of about 0.2%

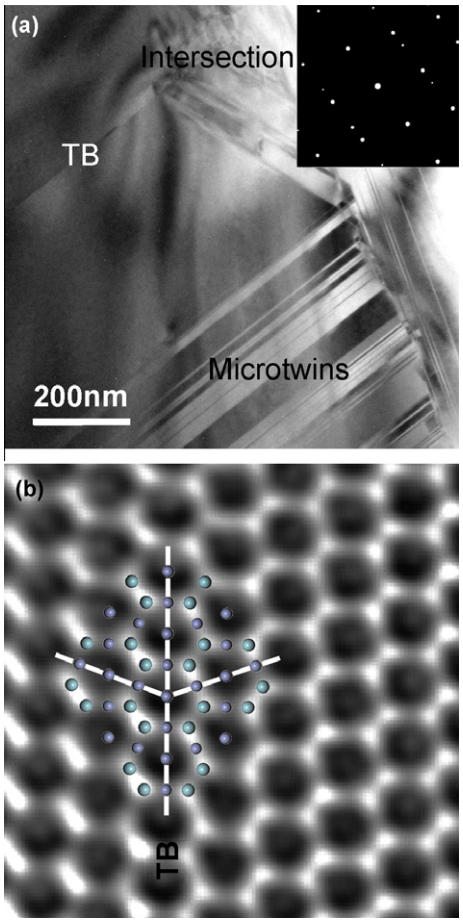

Fig. 2. (a) TEM image with an SAED pattern showing microtwins in the C15 Cr_2Nb and (b) HRSTEM annular dark-field image showing the atomic structure of a TB.

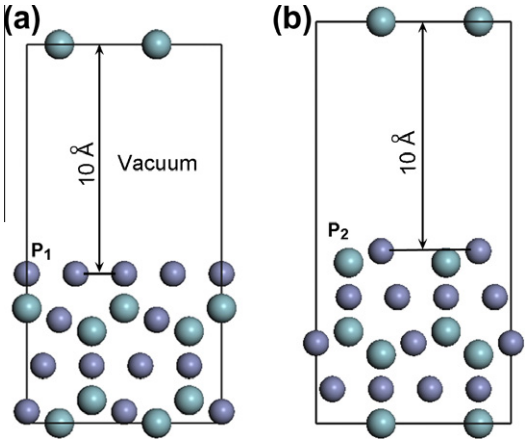

Fig. 3. [$\bar{1}$ 1 0] projection of cleavage models corresponding to fracture along (a) P_1 and (b) P_2, marked in Fig. 1b.

at a spatial resolution of ~2 nm [24]. Image distortions might also be introduced by the aberrations of the imaging system of the microscope and/or the camera used to acquire the images [25]. Regions free of dislocations, twins and SFs were used to evaluate the above systemic error, so that any artifacts would not be mistaken for distortions that arise from the defects.

2.3. First-principles calculations

Calculations were carried out using the CASTEP code [26]. For the exchange and correlation energy, the generalized gradient approximation was considered using the PBE functional [27]. For the sampling of the Brillouin zone, the calculations of total energy and the electronic structures used a $6 \times 6 \times 6$ k-point grid, and the cleavage energy used a $4 \times 4 \times 1$ grid. We used a plane-wave cutoff energy of 360 eV. The total energies were converged up to 0.6×10^{-6} eV. The calculated lattice parameter of the bulk C15 Cr_2Nb is 6.94 Å, which agrees well with the experimental value of 6.99 Å.

3. Results

3.1. Cleavage fracture from first-principles

Intrinsic cleavage fracture will take place when the applied mechanical energy exceeds the ideal cleavage energy, which is defined as the energy necessary to separate the crystal into two semi-infinite parts. We calculated the case of ideal brittle cleavage in which no relaxation was considered in the atomic positions after cleaving. Calculations without the structural relaxation after cleavage may overestimate the cleavage energy, but it will not influence the qualitative comparison between different lattice planes in the same crystal. The critical stress is calculated according to the universal binding energy relation [28], in order to evaluate the bonding strength.

Cleavage fracture occurs preferentially along {1 1 1} planes in C15 Cr_2Nb [10]. There are two possible cleavage planes as indicated by P_1 and P_2, as shown in Fig. 1b. Fig. 3 shows the [$\bar{1}$ 1 0] atomic projection of the two models corresponding to cleavage along planes P_1 and P_2, respectively. The thickness of the vacuum layer is set at 10 Å, which is much larger than the critical length [28] of ~0.6 Å, so that the interaction between the two surfaces could be neglected. The calculated ideal cleavage energy and critical stress are summarized in Table 1. The calculated ideal cleavage energy ($G_c = 6.65$ J m^{-2}) and critical stress ($\sigma_c = 40.78$ GPa) for cleavage fracture along plane P_1 are smaller than the corresponding values for cleavage along P_2 ($G_c = 7.20$ J m^{-2} and $\sigma_c = 44.37$ GPa, respectively). Therefore, fracture would prefer to take place along

Table 1
Calculated cleavage energy G_c and critical stress σ_c.

Cleavage location	G_c (J m^{-2})	σ_c (GPa)
P_1	6.65	40.78 ± 0.40
P_2	7.20	44.37 ± 0.44
Ideal TB	6.56	38.66 ± 0.38
Dilated TB	5.96	33.41 ± 0.33

plane P_1 between a single layer of pure Cr and a triple layer, rather than along plane P_2 inside the Nb–Cr–Nb triple layer.

3.2. Quantitative HRTEM

3.2.1. Crystal defects and strain mapping

Fig. 4a is an HRTEM image of a region containing some planar defects that intersect. Image simulations indicate that the bright spots in the HRTEM image correspond to Cr columns at the intersections between (1 1 1) and (1 1 $\bar{1}$) single layers composed of pure Cr atoms. The (1 1 1) and (1 1 $\bar{1}$) planar defects were respectively SFs and TBs, as indicated by lines. Fourier transform treatments of the HRTEM image were performed, as shown in Fig. 4b and c. By selecting the pair of reflection vectors of $\mathbf{g}_{11\bar{1}}$ and $-\mathbf{g}_{11\bar{1}}$, an inverse Fourier transform was performed to show the non-screw dislocations, as shown in Fig. 4c. In the inverse Fourier transform, the SFs indicated in Fig. 4a were in the form of jogs in the (1 1 $\bar{1}$) planes within the regions marked by rectangles 1 and 2, respectively. One non-screw dislocation is associated with the SF marked by rectangle 1 and the other is below rectangle 2, as indicated by arrows.

A Thompson's tetrahedron, a schematic top view of the Nb–Cr–Nb triple layer and the [$\bar{1}$ 1 0] projection of the atomic model of an SF are given in Fig. 5, in order to describe the dislocation dissociations and synchroshear motion of Shockley partials. Shear in Laves phase is accompanied by chemical rearrangement inside the triple layer. Slip and twinning are believed to occur inside the triple layers, rather than between the triple layer and the single Cr layer, via synchroshear [29–32]. Synchroshear consists of two shears in different directions on adjacent atomic planes. One Shockley dislocation glides between the lower atom level ($\boldsymbol{\beta}$) and the center ($\mathbf{a}$) with one Burgers vector and the other glides between the center ($\mathbf{a}$) and the upper level (γ) with a different Burgers vector. The three permitted glide directions for the upper level Nb atoms (γ) are $\boldsymbol{A\delta}$, $\boldsymbol{B\delta}$ and $\boldsymbol{C\delta}$, respectively. If the lower Nb atoms ($\boldsymbol{\beta}$) are fixed, and at the same time the upper Nb atoms (γ) move in the direction of $\boldsymbol{C\delta}$ (for example, atom γ_1 moves to the position above atom $\mathbf{a}_0$, Fig. 5b [30]), atom $\mathbf{a}_0$ will have to move in a direction of either $\boldsymbol{\delta A}$ or $\boldsymbol{\delta B}$. The net result of the above synchronized motion is that the triple layer stacking is changed from $\boldsymbol{\beta a\gamma}$ to $\boldsymbol{\beta c\alpha}$ to form an SF, as shown in Fig. 5c.

Fig. 6 shows enlarged HRTEM images for the two rectangle regions with SFs in Fig. 4. The construction of

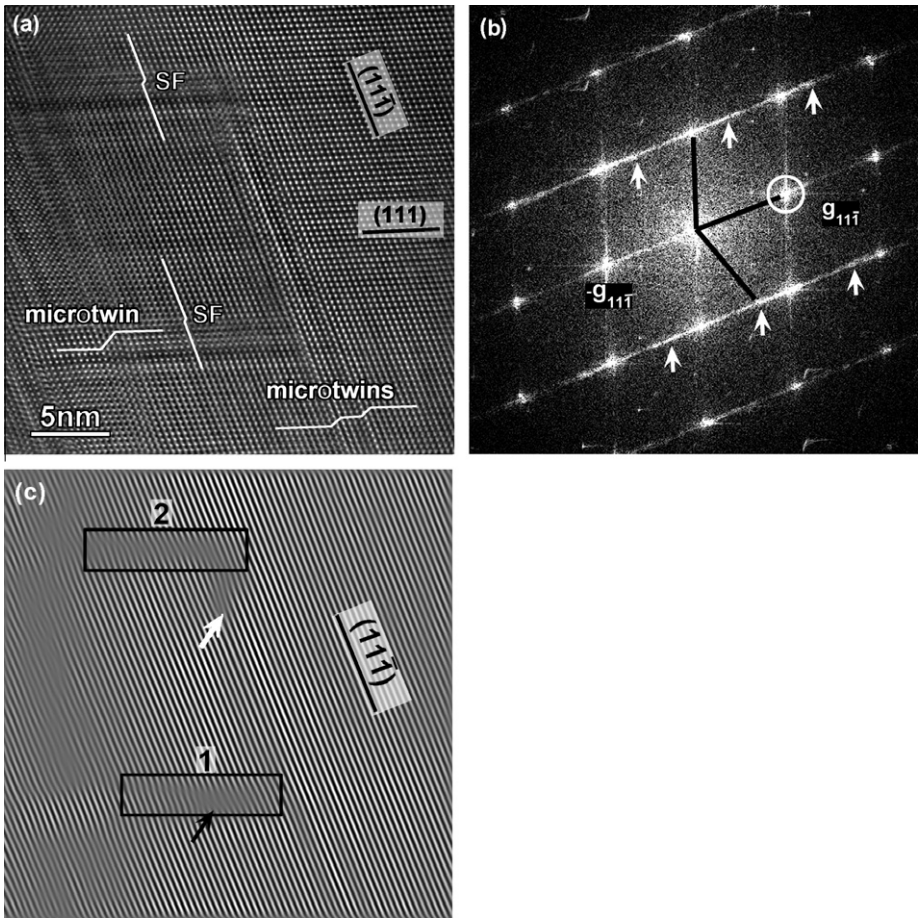

Fig. 4. (a) [$\bar{1}$ 1 0] HRTEM image showing SFs and TBs on (1 1 1) and (1 1 $\bar{1}$) planes, as indicated by black lines. (b) Fourier transform of the HRTEM image. The white arrows point to weaker reflections from microtwins. (c) Inverse Fourier transform using vectors $\mathbf{g}_{11\bar{1}}$ and $-\mathbf{g}_{11\bar{1}}$, showing the presence of non-screw dislocations, as indicated by arrows.

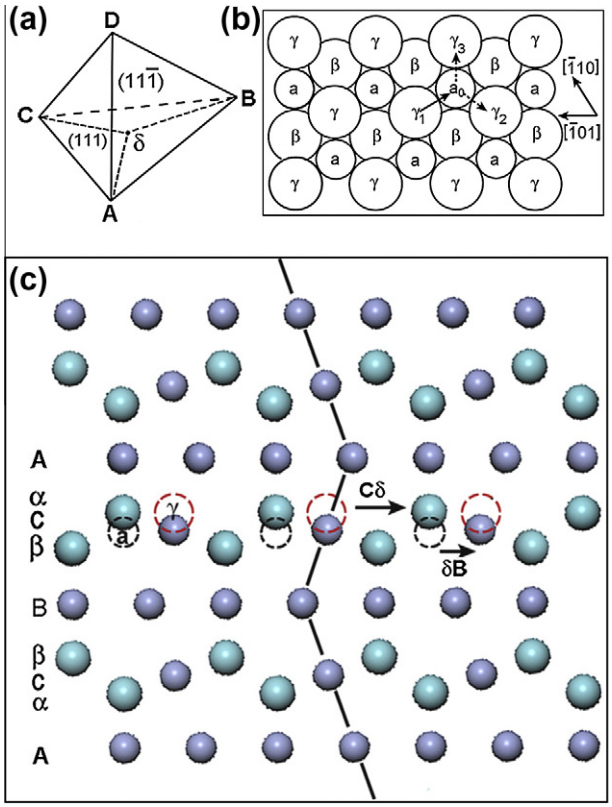

Fig. 5. (a) Thompson's tetrahedron, (b) a schematic plan view of the Nb–Cr–Nb triple layer and (c) [$\bar{1}$ 1 0] projection of an SF.

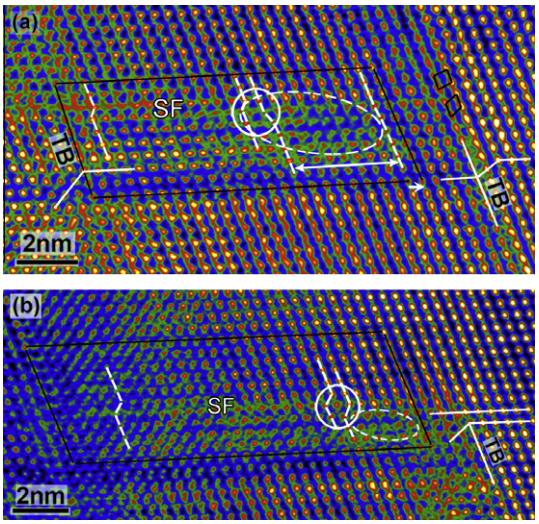

Fig. 6. Enlarged HRTEM images for regions marked by (a) rectangle 1 and (b) rectangle 2 in Fig. 4c, respectively. The white arrow indicates the closure failure of the Burgers circuit. The white circles indicate the core region of Shockley partials. The two black parallelograms in (a) show the structural transition from a 92° parallelogram to a 70.5° diamond along the TB.

a Burgers circuit surrounding the SF in region "1" (Fig. 4c) shows closure failure, as indicated by the white arrow in Fig. 6a. The corresponding Burgers vector is determined to be $\boldsymbol{CA}$ (1/2[1 0 $\bar{1}$]) or $\boldsymbol{CB}$ (1/2[0 1 $\bar{1}$]), which indicates that this SF originates from the dissociation of a perfect 60° dislocation into two Shockley partials having 30° and 90° characters respectively ($\boldsymbol{CA} = \boldsymbol{C\delta}$ (90°) + $\boldsymbol{\delta A}$ (30°) or $\boldsymbol{CB} = \boldsymbol{C\delta} + \boldsymbol{\delta B}$ (30°)). The dislocation marked by a solid circle at the right border of the SF in Fig. 6a is a 90° edge partial. This defect is the feature identified by the black arrow in the inverse Fourier transform in Fig. 4c. In Fig. 6a the 30° partial has arrived at and interacted with the left TB, but the 90° pure edge partial stayed about 5 nm in front of the right TB. The dislocation–TB reaction results in severe lattice distortion, as evidenced by the complex contrast with some extra bright spots and changes in shape and intensity of the bright spots in the vicinity of the intersection. The lower right region of the 90° pure edge partial (solid circles) is severely distorted, as indicated by the dashed ellipses. The misfit of the (1 1 $\bar{1}$) planes below and above the slip plane decreases gradually from left to right within the region indicated by the double-head arrow, and vanishes at a position of 4 (1 1 $\bar{1}$) planes in front of the TB. The observed asymmetrical lattice distortion is not consistent with the theoretical strain field of the dislocations [33], implying that other structural and/or chemical modifications have occurred nearby the dislocation. It is proposed that the lattice distortion is due to occurrence of chemical disordering in the slip plane or even in the adjacent lattice planes. This will be further studied by first-principles calculations, as shown later in Fig. 10. In addition, the two black parallelograms in Fig. 6a show the structural transition along the TB, which will be discussed in Section 3.2.2.

Fig. 6b is an enlarged HRTEM images for region 2 in Fig. 4, showing no closure failure of the Burgers circuit, which demonstrates that this SF was a result of the dissociation of a perfect screw dislocation into two 30° Shockley partials ($\boldsymbol{AB} = \boldsymbol{A\delta} + \boldsymbol{\delta B}$). The poor quality and abnormal contrast in the left part of the HRTEM image is mainly due to severe lattice distortion resulting from a high density lattice defects. The 30° Shockley partial (indicated by a solid circle) at the right side of the SF is about 5 nm away from the microtwin tip. The region indicated by the dashed ellipse is severely distorted, which is similar to the 90° partial shown in Fig. 6a. The lattice distortion in the region below the bottom right corner of the Burgers circuit is induced by the array of Shockley partials at the microtwin tip. The observed lattice distortion associated with the 90° partial and the 30° partial marked by solid circles in Fig. 6 will be further investigated by the combination of GPA and first-principles calculations.

Fig. 7 is an enlarged HRTEM image of the dislocation indicated by the white arrow in Fig. 4c. The dislocation indicated by the symbol "⊥" is just adjacent to the TB. The construction of a Burgers circuit surrounding the dislocation shows closure failure, as shown by the white arrow. The projected magnitude of the Burgers vector is equal to the distance between two neighboring Cr columns in the HRTEM image, indicating the presence of a 60° perfect dislocation in a (1 1 1) plane in the twin band. The

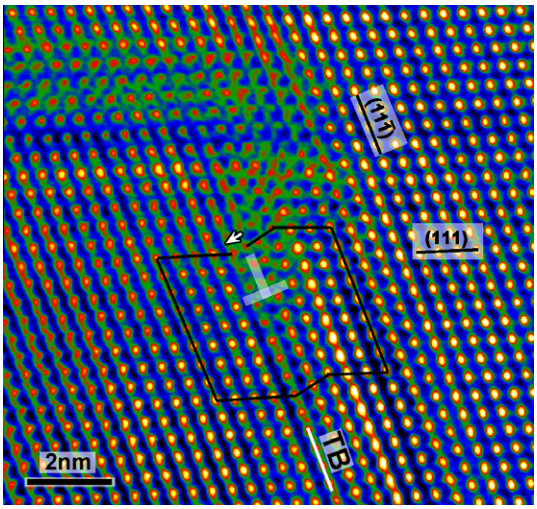

Fig. 7. HRTEM image showing a 60° perfect dislocation arrived at a TB.

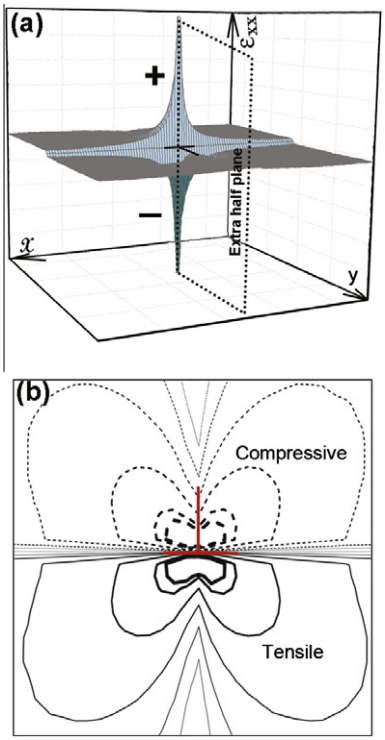

Fig. 8. Calculated ε_{xx} for a simple edge dislocation: (a) three-dimensional view; (b) two-dimensional contour. Symbol "⊥" and the dotted plane show the core position and the extra half plane of the edge dislocation, respectively. The magnitude of strain is qualitatively proportional to the line width in (b).

lattice strain of this 60° perfect dislocation will be investigated by the GPA technique and image simulations.

The strain fields revealed in the HRTEM images for non-screw dislocations show only the contribution from the edge component, when imaged along the dislocation line. Therefore, ε_{xx} of the theoretical strain fields for an edge dislocation is calculated and shown in Fig. 8, in order to compare with the measured strain based on experimental HRTEM images using the GPA method. The ε_{xx} has mirror symmetry about the extra half atomic plane.

Before the GPA strain analysis, Wiener filtering was performed on the HRTEM images to improve the image quality [34]. In principle, both the in-plane strain tensor ($\boldsymbol{\varepsilon}_{ij}$) and rigid-body rotation ($\boldsymbol{\omega}_{ij}$) can be obtained by the GPA technique. Here we will focus on the lattice strain perpendicular to the $(1\,1\,\bar{1})$ TB plane, since TBs are planar obstacles to incident dislocations. Fig. 9a is a GPA strain map obtained by using the reflection vector $\mathbf{g}_{11\bar{1}}$ in Fig. 4b. Positions of the three dislocations emphasized in Figs. 6 and 7 are indicated by their characteristic parameters (90°, 30° and 60°) aside the corresponding centers of strong local strain fluctuation in the strain map. An abrupt change in color is present in regions with dislocations, showing a change in sign of strain across the dislocation core, which is consistent with theory [33]. However, the strain field of the 90° partial dislocation is remarkably distorted, deviating significantly from the theoretical ε_{xx} for an edge dislocation (Fig. 8). The GPA strain mapping results are qualitatively consistent with the asymmetrical lattice distortion around the dislocation core as directly observed from the HRTEM image in Fig. 6. Additionally, it is surprising to see an extremely long tail (>10 nm) in the region under tensile strain below the 60° dislocation, which deviates far from theory (Fig. 8). Moreover, the compressive part of the strain field of the 60° perfect dislocation was repulsed away from the TB. The abnormal lattice strains of the 60° dislocation will be modeled and explained in Section 3.2.2 and the discussion section. Due to the extremely high density of defects, the lattice distortion in the left part of the HRTEM image is too high to be evaluated by the GPA method and therefore will not be discussed.

Fig. 9b and c shows the strain profile along the arrows in the two rectangles "1" and "2" parallel and perpendicular to the TB plane, respectively. The averaged strain values change immediately from negative (compressive) to positive (tensile) across the 60° dislocation core (Fig. 9b). The tensile strain drops sharply within a distance of about 1 nm, levels off at about 2.5% within a range of 10 nm, starting from a position 2 nm away from the dislocation core, then decreases gradually to zero. In Fig. 9c the peak centered at ~5 nm has a full width at half maximum of less than 1 nm, which indicates that the lattice dilatation is confined within a quite narrow slice, with a width of about twice the $(1\,1\,\bar{1})$ spacing. Statistical analysis indicates that the matrix regions free of dislocations on both sides of rectangle "1" have average strains of $-0.04 \pm 0.28\%$, indicating a noise level of about 0.28% in the strain map. The measured values of local strains are more than six times the standard deviation, as shown in Fig. 9b and c, and thus the measured local strains are true rather than noise. The influence of contrast delocalization has to be considered for the microtwin regions, in order to verify the contribution of real microstructural features to the prolonged tail. The contrast delocalization on the lattice images of this

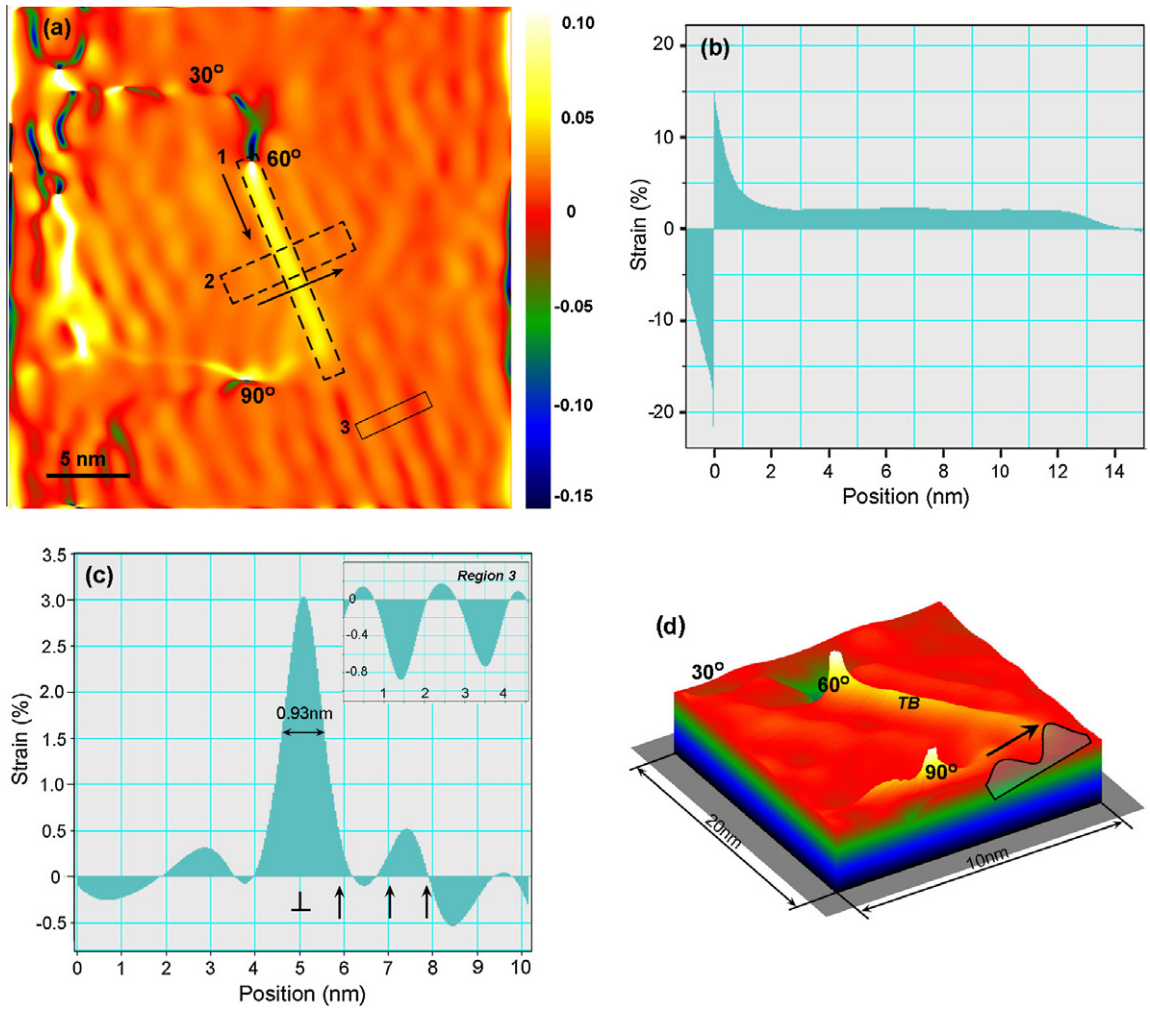

Fig. 9. (a) GPA strain distribution using reflection $\mathbf{g}_{11\bar{1}}$. (b and c) Profiles of strain distribution averaged over the width of rectangles 1 and 2 in (a), respectively. The strain distribution in rectangle 3 is shown as an inset in (c), in order to compare it with that in rectangle 2. The positions of TBs are indicated by "⊥" and arrows in (c). Note that, among the four TBs, real lattice dilatation was detected only within a segment of the one just adjacent to the 60° perfect dislocation. (d) Three-dimensional view of local strain morphology with the same scale as (a); the inset shows the strain distribution along the arrow.

TB and other neighboring defects (TBs and SFs) should be at the same level. The inset in Fig. 9c illustrates strain distribution in region "3" with several TBs but no dislocation, showing strain values in a range from −0.8% to 0.2%. Also, no obvious lattice dilation is detected along the other three TBs indicated by arrows on the right side of this TB, as shown in Fig. 9c. Therefore, the prolonged tail of strain is determined to be the result of real lattice dilatation and not an experimental artifact due to contrast delocalization in the HRTEM image. The variation of local lattice parameters along the TB will be described in some detail in the next section.

A three-dimensional view of the strain distribution in a 10 nm × 20 nm region is shown in Fig. 9d. This view of the contour surface of the strain map makes it easier to see the interactions between the dissociated partial dislocations (30° and 90°) and their neighboring lattice defects (twinning partials and TB), as demonstrated by the overlap of their strain fields (e.g. the inset showing the interaction between the 90° partial dislocation and the TB).

According to the synchroshear model, the partial dislocation core has an extra column of Cr atoms [30,32], which must affect the local strain field of the core. As shown in Fig. 5b, if atom γ_1 (Nb) represents the moving front of the partial dislocation and its movement ($\boldsymbol{C\delta}$) will push atom $\mathbf{a}_0$ (Cr) to move in the direction $\boldsymbol{\delta A}$, a local extra Cr atom will appear below or around atom γ_2 (Nb). In principle, an efficient way to evaluate the effect of the extra Cr atom on the local lattice geometry is first-principles optimization. However, such calculations are not practical at this time, since a proper model will need many hundreds of atoms for this complex material, which is beyond the capability of our computing resources. Fig. 10 shows a small model structure that illustrates the general effect of a Cr interstitial on the local lattice in a semi-quantitative way. The Cr interstitial below the Nb atom is not stable,

and tends to move away from the triple Nb–Cr–Nb layer toward the pure Cr plane, as indicated by the arrow in Fig. 10b. This is likely due to the facts that (i) the kagome single layer is composed of smaller Cr atoms and (ii) the spacing between the single Cr layer and the triple Nb–Cr–Nb layer is three times that of the interplanar spacing within the triple layer. The deviation of the Cr atom from its original slip plane based on first-principles calculations is consistent with the observed asymmetrical form of lattice distortion near the cores of partial dislocations, as shown in Fig. 6. The observed asymmetrical lattice distortion nearby the partial dislocation cores (Fig. 6) is thus related to the occurrence of short-range redistribution of the excess Cr atoms in front of the dislocations, as compared with the symmetrical strain field (Fig. 8) for a simple dislocation core [33]. The interactions between neighboring dislocations or TB should also play some role in the observed distorted strain fields of the 30° and 90° partial dislocations. Not only are large displacements of neighboring atoms seen, but also a significant change in unit cell parameters is observed ($a = 7.356$ Å, $b = 7.104$ Å, $c = 7.352$ Å; $\alpha = 89.73°$, $\beta = 86.48°$, $\gamma = 89.81°$). Larger lattice distortions can be reasonably expected if the lattice strain of a partial dislocation is also taken into account.

3.2.2. Atomistic model and image simulation for lattice dilatation along TB

Fig. 11 shows enlarged HRTEM images for the microtwin regions "2" and "3" with and without the lattice dilatation shown in Fig. 4, respectively. Within the prolonged lattice dilatation region along the TB, a characteristic quadrilateral connecting four Cr columns in the TB plane and the neighboring pure Cr $(1\,1\,\bar{1})$ plane is seen in Fig. 11a to be a 92° parallelogram rather than the standard 70.5° diamond for fcc structures. Direct measurements on the HRTEM image also demonstrate that the dilatation occurs between the TB and the adjacent Cr $(1\,1\,\bar{1})$ on its right side (Fig. 11a). Distances between adjacent intensity features outside of this region are not changed from those seen in the bulk structure. Therefore, it is concluded that a single monoclinic layer appears between the TB and its right neighboring $(1\,1\,\bar{1})$ Cr plane in Fig. 11a. No such deviation was observed in region "3" without lattice dilatation perpendicular to the TB (Fig. 9b).

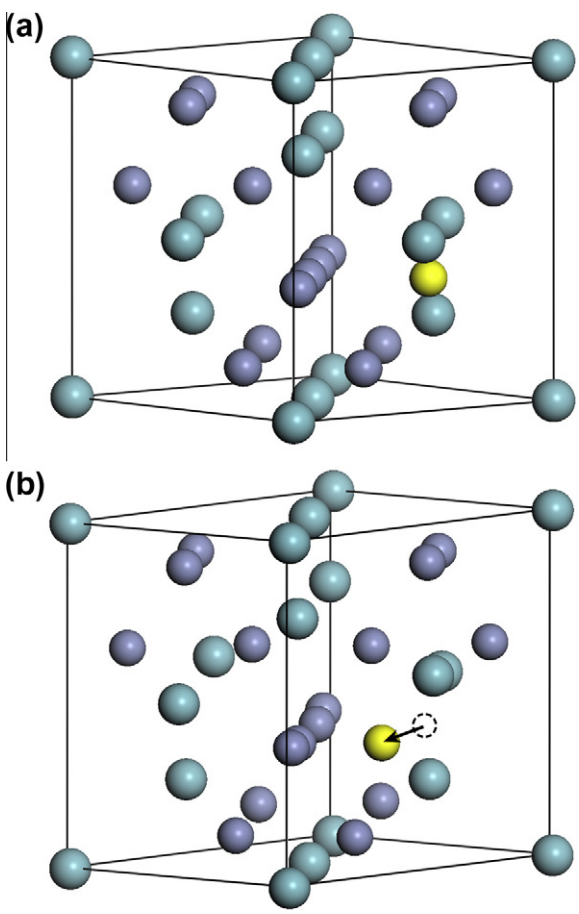

Fig. 10. Effect of Cr interstitial (yellow): (a) before and (b) after geometry optimization. The dashed circle indicates the original position of the Cr interstitial. (For interpretation of the references to colour in this figure legend, the reader is referred to the web version of this article.)

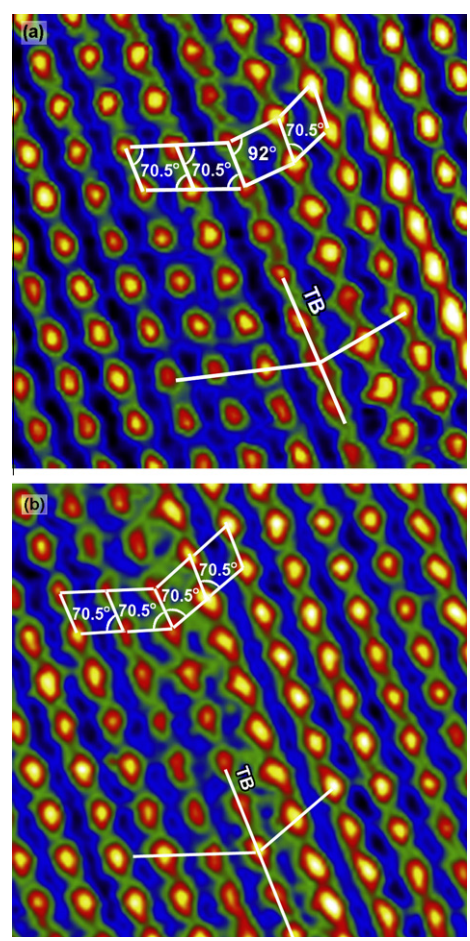

Fig. 11. (a) Enlarged HRTEM image showing that lattice distortion occurred within a region close to the 60° perfect dislocation at the TB in Fig. 7. (b) HRTEM image showing the structure of a normal TB.

Image simulations of the TB region were performed in order to understand the origin of the observed lattice distortions. Based on HRTEM observations (Fig. 11a) and the prediction of cleavage between a pure Cr layer and the adjacent Nb–Cr–Nb triple layer according to first-principles calculations, atomic models were built up for the TB region by introducing a single monoclinic layer ($\mathbf{a}_M = \mathbf{a}_{C15} = 0.699$ nm, $\mathbf{c}_M = 0.430$ nm and $\boldsymbol{\beta} = 92°$). In order to eliminate the boundary effect in image simulation, the width on both sides of the TB is 10 times the unit cell of the C15 Cr_2Nb in the atomic models (1134 atoms in total, i.e. 756 Cr atoms and 378 Nb atoms). Fig. 12a shows the constructed model with an expansion of 0.3 Å (from 1.5 Å to 1.8 Å) between the pure Cr TB plane and the neighboring Nb layer, without considering any local relaxation, which corresponds to the cleavage model P_1 in Fig. 3. The spherical aberration coefficient of the objective lens is 1.2 mm for the microscope used. Fig. 12b is the simulated image for a sample thickness of 4.0 nm at a defocus value of 79 nm, which matches well with the experimental HRTEM image, as indicated by the corresponding 92° parallelogram. Both first-principles geometry optimization and image simulations on a perfect TB model do not show obvious lattice distortion. Therefore, the observed large lattice dilatation along the TB is attributed to the interaction of the incident 60° dislocation with the TB. The lattice dilatation terminates close to the (1 1 1) plane with the SF bounding a 90° Shockley dislocation (Figs. 6 and 7). The strain field of the 90° Shockley dislocation overlaps with the tip of lattice dilatation along the TB (Fig. 9d), demonstrating repulsion between the dislocation and the TB. Therefore, the termination of lattice dilatation along the TB is attributed to the interaction between the 90° Shockley dislocation and the TB.

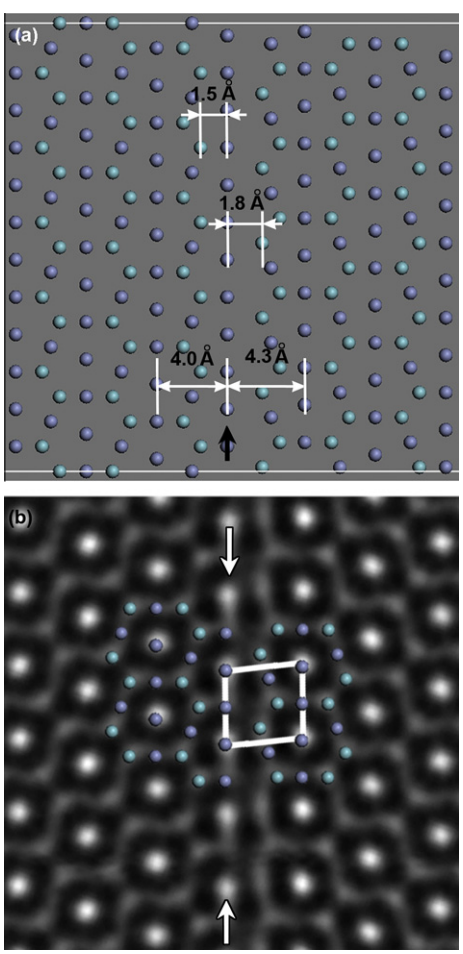

Fig. 12. (a) Atomic model for the observed lattice dilatation along a TB; (b) a simulated HRTEM image. The black arrows indicate the TB position, and the dotted lines show the (1 1 1) and $(1\,1\,1)_T$ planes.

4. Discussion

The crystal defects observed in the present C15 Cr_2Nb samples were probably formed at relatively high temperatures during the solidification and/or cooling process driven by thermal stress [35]. Nanometer-scale regions of severe lattice distortion are often observed in the vicinity of dissociated Shockley partials and TB–SF intersections. In the distorted regions, not only are the bright features not in their ideal positions, but their shape and intensity are also significantly different. We find long-range perturbation of dislocation strain fields consistent with chemical disordering. Weertman [36] proposed a theory of viscous motion of dislocations in ordered intermetallics to explain their good creep resistance, assuming that dislocation motion may result in local damage of structural and/or chemical ordering. The dislocation motion takes place inside the Nb–Cr–Nb triple layer in the form of synchro-shear [29–32], which introduces excess Cr atoms in front of the moving dislocation core. These Cr atoms need to diffuse with the moving dislocation core. The dislocation mobility and mean free path must be reasonably high above the ductile–brittle transition temperature (DBTT) [37], when the chemical disorder can be repaired via thermally driven diffusion of the excess Cr atoms. The nanometer scale distorted regions associated with Shockley partials in the C15 Cr_2Nb were retained due to the loss of diffusivity at a certain temperature below the DBTT, and at the same time the partial dislocations could no longer move, although the thermal stress was still present. At low temperatures, dislocation motion, even as little as one Burgers vector of the Shockley partial, will result in short-range lattice distortions and/or chemical disordering. As shown in Fig. 10, these effects are due to the extra column of Cr that can no longer diffuse with the moving dislocation core. Chemical disordering can weaken local bonding strength [38]. Therefore, the extended perturbed strain field resulting from chemical disordering surrounding the dislocation core (Fig. 6) could eventually under sufficient stress initiate cracking.

Twins are widely present in C15 Cr_2Nb due to its moderate SF energy [5,8,11,18]. Importantly, a large lattice dilatation (~0.3 Å, Figs. 9 and 11) along the TB is seen to be introduced by the presence of a single incident 60°

dislocation. This is important because the TBs in the C15 Cr_2Nb are single Cr layers, as seen in Fig. 2, and because first-principles calculations show fracture cleavage occurs preferentially between the Cr single layer and the Nb–Cr–Nb triple layer, as seen in Fig. 3. Also, first-principles calculations indicate that the TB in the C15 Cr_2Nb ($G_c = 6.56$ J m^{-2}, $\boldsymbol{\sigma}_c = 38.66$ GPa) is slightly weaker than that in the bulk ($G_c = 6.65$ J m^{-2}, $\boldsymbol{\sigma}_c = 40.78$ GPa). Importantly, when there is a lattice dilatation of 0.3 Å along the TB, the cleavage energy and critical stress are further decreased, to $G_c = 5.96$ J m^{-2} and $\boldsymbol{\sigma}_c = 33.41$ GPa, respectively (Table 1). Therefore, the long and relatively wide lattice dilatation along the TB produced by only one incident dislocation can be reasonably expected to be a weak link in the material. The dilated region associated with the TB/dislocation interaction is expected to become wider and longer as additional dislocations pile-up at the boundary. Therefore the TBs may serve as nucleation sites for cracks. These dilated TBs should also readily propagate cracks in the C15 Cr_2Nb, similar to what is seen in corundum [20] and Mg alloys [21].

5. Conclusions

- HRTEM observations and GPA strain analyses show that there are asymmetrical nanoscale distorted regions in the vicinity of Shockley partial dislocations. First-principles calculations indicate that the disturbed strain fields should be related to the presence of excess Cr atoms associated with the synchroshear inside the Nb–Cr–Nb triple layers. This chemical and structural inhomogeneity would be expected to significantly impede the motion of dislocations, and thus the ductility of C15 Cr_2Nb.
- First-principles calculations of ideal cleavage energy show that cleavage fracture occurs preferentially between a pure Cr layer and the adjacent Nb–Cr–Nb triple layer, rather than inside the triple layer.
- HRTEM observations demonstrate that an incident 60° dislocation can result in a large lattice dilatation along the TB, suggesting that TBs in C15 Cr_2Nb may nucleate and propagate cracks readily, which contributes to its poor toughness.

Acknowledgements

Z.Q.Y. would like to thank Prof. Y.M. Wang for discussion and Z. Li for help in writing the GPA code. This work was supported by the NSFC (51171189, 50771096) and the MoST of China (2009BC623705). Z.Q.Y. is also supported by a CAS visiting scholarship. M.F.C. and S.J.P. are supported by the Office of Basic Energy Sciences, Materials Sciences and Engineering Division of the US Department of Energy.

References

[1] Taub AI, Fleischer RL. Science 1989;243:616.
[2] Anton DL, Shah DM. Mater Sci Eng A 1992;l53:410.
[3] Takasugi T, Yoshida M, Hanada S. Acta Mater 1996;44:669.
[4] Zhang W, Yu R, Du K, Cheng ZY, Zhu J, Ye HQ. Phys Rev Lett 2011;106:165505.
[5] Kazantzis AV, Aindow M, Jones IP, Triantafyllidis GK, De Hosson JTM. Acta Mater 2007;55:1873.
[6] Chu F, Thoma DJ, Kotula PG, Gerstl S, Mitchell TE, Anderson IM, et al. Acta Mater 1998;46:1759.
[7] Kazantzis AV, Aindow M, Jones IP. Mater Sci Eng A 1997;233:44.
[8] Hong S, Fu CL, Yoo MH. Philos Mag 2000;A80:871.
[9] Ormeci A, Chu F, Wills JM, Mitchell TE, Albers RC, Thoma DJ, et al. Phys Rev B 1996;54:12753.
[10] Li CL, Wang B, Li YS, Wang R. Intermetallics 2009;17:394.
[11] Chu F, He Y, Thoma DJ, Mitchell TE. Scripta Mater 1995;33:1295.
[12] Rosch F, Trebin HR, Gumbsch P. Int J Fract 2006;139:517.
[13] Aufrecht J, Leineweber A, Duppel V, Mittemeijer EJ. J Mater Res 2010;25:1983.
[14] Vedmedenko O, Rosch F, Elsaser C. Acta Mater 2008;56:4984.
[15] Moran JB. Trans Met Soc AIME 1965;233:1473.
[16] Saka H, Hayakawa T, Nakamura M, Mizutani H, Nakamura E. Philos Mag A 1993;68:871.
[17] Botton GA, Humphreys CJ. Intermetallics 1999;7:829.
[18] Yoshida M, Takasugi T. Intermetallics 2002;10:85.
[19] Argon AS, Orowan E. Philos Mag 1964;9:1023.
[20] Pugh SF. Brit J Appl Phys 1967;18:129.
[21] Cizek P, Barnett M. Scripta Mater 2008;59:959.
[22] Stadelmann PA. Ultramicroscopy 1987;21:131.
[23] Hÿtch MJ, Snoeck E, Kilaas R. Ultramicroscopy 1998;74:131.
[24] Hÿtch MJ, Putaux JL, Thibault J. Philos Mag 2006;86:4641.
[25] Hüe F, Johnson CL, Lartigue-Korinek S, Wang G, Buseck PR, Hÿtch MJ. J Electr Microsc 2005;54:181.
[26] Segall MD, Lindan PJD, Prober MJ, Pickard CJ, Hasnip PJ, Clark SJ, et al. J Phys Condens Matter 2002;14:2717.
[27] Perdew JP, Burke K, Ernzerhof M. Phys Rev Lett 1996;77:3865.
[28] Rose JH, Smith JR, Ferrante J. Phys Rev B 1983;28:1835.
[29] Allen CW, Delavigneete P, Amelinckx S. Phys Status Solidi A 1972;9:237.
[30] Hazzledine PM, Pirouz P. Scripta Metall Mater 1993;28:1277.
[31] Kronberg ML. Acta Metall 1957;5:507.
[32] Chisholm MF, Kumar S, Hazzledine P. Science 2005;307:701.
[33] Hirth JP, Lothe J. Theory of dislocations. New York: McGraw-Hill; 1968.
[34] Kilaas R. J Microsc 1998;190:45.
[35] Kumar KS, Liu CT. Acta Mater 1997;45:3671.
[36] Weertman J. J Appl Phys 1957;28:1185.
[37] Kazantzis AV, Aindow M, Triantafyllidis GK, De Hosson JTM. Scripta Mater 2008;59:788.
[38] Cahn RW. Mater Sci Eng A 2002;324:1.